AIAA JOURNAL
Vol. 43, No. 5, May 2005

Calibration and Data-Reduction Algorithms for Nonconventional Multihole Pressure Probes

Vijay Ramakrishnan* and Othon K. Rediniotis†
Texas A&M University, College Station, Texas 77843-3141

The development of calibration and data-reduction algorithms for nonconventional multihole pressure probes is presented. The algorithms that have been developed in the past for conventional five- and seven-hole probes are not optimal for probes with port arrangements (on the probe tip) that are nonconventional. Conventional algorithms utilize the axisymmetry of the port distribution pattern to define the nondimensional pressure coefficients. These coefficients are typically defined specifically for these patterns, but fail to represent correctly different patterns of port arrangements, such as patterns without axisymmetry or regularity. The algorithms introduced can handle any pattern of port arrangement, from axisymmetric and regular to random. Moreover, they eliminate the need to separate the measurement domain of a probe to low-angle and high-angle regimes, typical in conventional five- and seven-hole-probe algorithms that require two different sets of pressure coefficient definitions and procedures. Additionally, the algorithms have been formulated such that they facilitate redundancy implementations, especially in applications where such redundancy is important, such as air-data systems. The developed algorithms are applied to a nonconventional probe, a nearly omnidirectional 18-hole probe, and demonstrate very high flow-measurement accuracy.

Nomenclature

A_θ, B_θ	=	polynomial coefficients for C_θ expression
A_ϕ, B_ϕ	=	polynomial coefficients for C_ϕ expression
Cp	=	pressure coefficient
C_s	=	static pressure coefficient
C_t	=	total pressure coefficient
C_θ	=	cone-angle coefficient
C_ϕ	=	roll-angle coefficient
d	=	Euclidean distance
P_s	=	static pressure
P_t	=	total pressure
q	=	freestream dynamic pressure
R, S, T	=	polynomial coefficients for q_{est}
T_s	=	static temperature
T_t	=	total temperature
U	=	velocity magnitude at measurement point
u	=	velocity magnitude at pressure port
α	=	pitch angle
β	=	yaw angle
$\Delta P1$	=	difference in port pressures, $P_1 - P_3$
$\Delta P2$	=	difference in port pressures, $P_2 - P_3$
$\Delta P3$	=	difference in port pressures, $P_3 - P_4$
Θ	=	cone angle in global coordinate system
θ	=	cone angle in local coordinate system
θ_0	=	polynomial coefficient for θ expression
λ	=	scaling factor
ρ	=	density of air
Φ	=	roll angle in global coordinate system
ϕ	=	roll angle in local coordinate system
ϕ_0	=	polynomial coefficient for ϕ expression
ψ	=	central angle between any two points on a sphere

Subscripts

cal	=	from calibration database
est	=	estimated value
i	=	port number
max1	=	port number with highest pressure
max2	=	port number with second-highest pressure
max3	=	port number with third-highest pressure
x, y, z	=	coordinate direction

Introduction

MULTIHOLE pressure probes have, over the years, been used to resolve the three-dimensional velocity vector and static and total pressures at the point of measurement in a flowfield. Such devices include 5- and 7-hole probes[1–5] and 18-hole, nearly omnidirectional probes.[6] There are, of course, other types of pressure probes such as pitot-static probes and yaw probes that, however, are not of interest here because they cannot resolve all three components of the velocity vector.

Numerous calibration and data-reduction algorithms and procedures have been developed over the years for steady measurements with typical five- and seven-hole probes. One of the approaches relates the flow velocity magnitude and incidence angle to a theoretical model, such as a potential flow model. Based on the theoretical model, the port pressures are related to the flow incidence and velocity magnitude. Kjelgaard[3] used this technique on a hemispherical-tipped five-hole probe. However, the fact that the measurement accuracy expected from multihole probes has dramatically increased over the years (often better than one-quarter degree in the flow angles and one-half a percent in the velocity magnitude) has eliminated this theoretical approach as a viable candidate, especially for small probe sizes [$\frac{1}{8}$-in. (3.175-mm) tip diameter or smaller], where manufacturing imperfections are inevitable. For small probes, nonnulling methods are best suited. These methods are based on extensive calibration of the probe and allow for imperfections in the probe tip geometry. The probe is calibrated in a flowfield with known properties where the probe is rotated through a range of angles to simulate every possible flow incidence angle resolvable by the probe. At each unique angular combination, the port pressures are recorded and stored in a database. Some early work includes that of Gettelman and Krause,[7] who determined the influence of the flow angle on static pressure measurements in subsonic flowfields using a two-hole wedge probe. Although they did not directly use it for

Received 22 April 2004; accepted for publication 15 November 2004.

*Graduate Research Assistant, Aerospace Engineering Department.
†Associate Professor, Aerospace Engineering Department. Associate Fellow AIAA.

angle predictions, they demonstrated the relationships that can be used for angle predictions. Centolanzi[8] used a 40-deg cone probe to determine the angle and speed in supersonic flows. Probe calibration is also discussed in Ref. 1, where details on a probe traversing apparatus are presented. Bryer and Pankhurst gave a comprehensive overview of probe types, design, and construction, as well as manometer systems for probes.

After the probe has been calibrated, the data are processed, and sets of nondimensional velocity-invariant coefficients are calculated that relate the relative magnitude of the port pressures to the flow incidence angle. Furthermore, a curve fit is used to relate these nondimensional coefficients to the angles and form explicit polynomial expressions.[5] Following the processing, the probe can be inserted into a flowfield with unknown velocity magnitude and angularity. The nondimensional pressure coefficients are calculated from the port pressures, and the flow angles are found directly from the polynomial expressions. A similar method is used to find the velocity magnitude.

There are a number of different approaches to the aforementioned procedure, varying in the definitions of the pressure coefficients and the method of curve fitting. The use of only one set of coefficient definitions limits the angular range the probe can resolve because, at high incidence angles, the flow over one or more of the ports may be separated. Based on a five-hole probe, Bryer and Pankhurst[1] divided the measuring region into a low-angle regime, corresponding to flow incidences resulting in the center port sensing the highest pressure, and four high-angle regimes, when one of the peripheral ports senses the highest pressure. This approach allows for region-specific coefficient definitions and extends the angular range of the probe. Gerner and Maurer,[9] Gerner and Sisson,[10] and Everett et al.[2,11] used seven-hole probes and split the angular domain into low-angle and high-angle flows (by methods similar to those used by Bryer and Pankhurst[1]) and extended the usable angular range up to 70 deg in cone angle (angle between the velocity vector and the probe axis). Based on the work by Gerner and Maurer,[9] Ostowari and Wentz[12] extended the angular range of a conical five-hole probe to 85 deg. However, no quantitative analysis of the errors in the high-angle range was given.

The polynomial fitting of the nondimensional coefficients to the flow angles has been studied extensively. Most early work used either a global procedure, where polynomials were created for all calibration points, or a sector-based procedure.[9] Rediniotis et al.[5] were able to increase accuracy by dividing the port-specific regions into several sections, thereby increasing the number of regions for which polynomials were used to describe the calibration coefficients. Houtman and Bannink[13] used a combined theoretical and experimental calibration on a hemispherical-tipped five-hole probe in high-subsonic to supersonic flows. Their prediction capabilities were good at low flow angles but deteriorated at cone angles larger than about 45 deg due to separation and shock wave effects. They also introduced a localized interpolation scheme using only eight calibration points for increased accuracy. Similar to the work by Houtman and Bannink,[13] Zilliac[4,14] and Johansen et al.[15] developed methods that are local in nature, where a calibration database is searched and interpolation or curve fitting is performed locally using only a few data points. Rediniotis and Vijayagopal[16] used artificial neural networks (ANN) rather than traditional polynomial fitting to relate the coefficients to the flow angles. Through extensive training, the ANN yielded very good prediction capabilities.

The definitions of the nondimensional coefficients are crucial to maximizing sensitivity and data-reduction accuracy, minimizing dependence on Mach and Reynolds numbers, and avoiding singularities. Clark et al.[17] calibrated hemispherical-tipped probes from high-subsonic flows up to Mach 2.0, examining five different calibration coefficient definitions for sensitivity to Mach number effects. They also compared 10 identically produced probes and found that individual calibrations were required for each single probe due to manufacturing idiosyncrasies. Takahashi[18] performed analysis on the coefficient behavior identifying singularities while also optimizing for processing speed.

Shepherd[19] introduced a four-hole cobra probe with tip shape similar to a five-hole probe, but with one central port and only three peripheral ports. Because there are only four independent quantities to be measured, the four-hole probe avoids redundant (pressure) information. Shepherd[19] calibrated and used this probe to resolve velocity and pitch and yaw angles with reasonable accuracy. However, he only used one set of coefficient definitions, which limited the angular range of the probe to $\pm$ 20 deg in pitch and yaw. The maximum flow incidence angle that can be resolved by a five- or seven-hole probe depends on the probe tip geometry and port locations. Most probes can accurately resolve angles up to approximately 70 deg. For many complex flowfields, the angular range in the measurement domain (either spatially, temporally, or both) is greater than what a five- or seven-hole probe can resolve, for example, the flow in the wake of a bluff body, and for such flows the omnidirectional probe (Fig. 1) is preferred.[6] The omniprobe is an extension of the five- and seven-hole probes with the distinct advantage that it can resolve flow angles up to 160 deg from its principal axis. Similar to the five-hole probe, the omniprobe predicts the flow angles, the local total and static pressures, and the velocity magnitude with a high degree of accuracy.

Recently, an optimization of the 18-hole probe, the 12-hole omnidirectional probe, has been developed.[20] The new 12-hole design offers several advantages over the previously developed 18-hole probe. That the new design has a 33% fewer number of holes has significant beneficial implications in the instrument's spatial resolution (smaller probe sizes), frequency response (larger internal tubing diameters), as well as cost of interfacing and usage. The new design has 12 pressure ports distributed on the surface of a spherical tip.

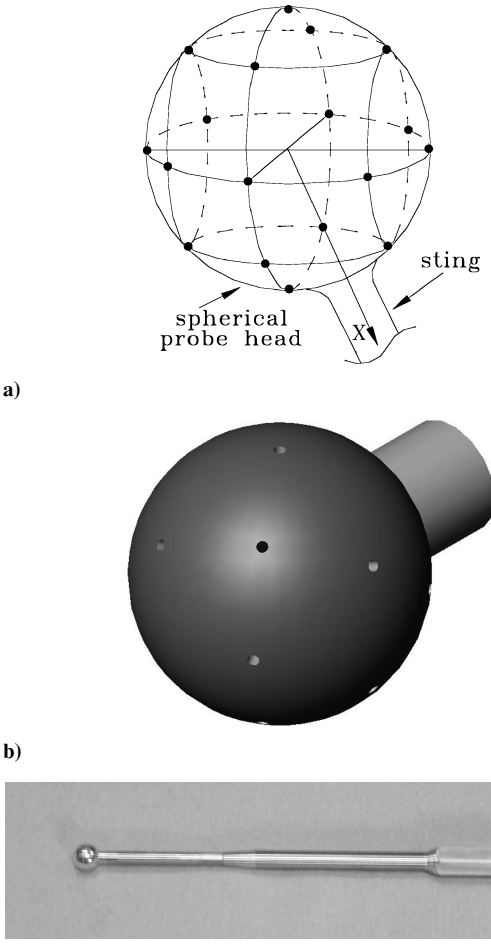

Fig. 1 Nearly omnidirectional 18-hole probe: a) port arrangement and grouping, b) isometric view showing spherical tip and cylindrical sting, and c) photograph showing a fully assembled 18-hole probe.

Its 12 ports are located at the corners of an icosahedron (canonical shape with 20 sides, each one of which is an equilateral triangle, and 12 corners) inscribed inside a sphere (Fig. 2). The new design is optimal in the sense that, regardless of the flow direction (and, thus, location of the stagnation point on the spherical tip), there are always at least four usable pressure ports in the attached flow region over the sphere. This allows the calculation of the four unknown flow quantities, that is, the two flow angles, the total pressure, and the static pressure, with the minimum necessary number of holes/ports on the probe tip.

However, newly developed multihole probes, such as the 18-hole and 12-hole probes, do not necessarily have the conventional port arrangements of the 5- or 7-hole probes. One of the challenges when working with a generic port arrangement is that the conventional definitions of the nondimensional pressure coefficients either can no longer be applied, or, if they can be applied, they may be far from optimal. Some of the important properties of a properly defined coefficient include independence from the other three variables (for example, the yaw angle coefficient should be independent of the pitch angle and the dynamic and static pressures) and smooth, preferably linear, behavior. As will be demonstrated later, conventionally defined coefficients do not necessarily exhibit these properties for nonconventional port arrangements. There is, therefore, the need for a systematic way of defining well-behaved coefficients for any port arrangement. Additionally, several conventional definitions and data-reduction methods lack considerations of redundancy and fault tolerance. Simple examples are the typical definitions of the flow angle coefficients for a five- or seven-hole probe in the low-angle regime. These definitions involve all five or seven port pressures. Therefore, even if one of the five or seven pressure sensors malfunctions, the conventional definitions fail, although the probe itself is still perfectly functional, at least in the low-angle regime, because only four ports are needed for the calculation of the flow quantities (two flow angles and total and static pressures).

In this work, we first present a systematic way of defining well-behaved pressure coefficients for any generic port arrangement (5-, 7-, 12-, 18-hole, or other) for spherical- or hemispherical-tipped probes. These definitions also take into account redundancy and fault tolerance considerations. Then, we develop a data-reduction algorithm for any generic port arrangement. Finally, we demonstrate the performance of the developed coefficients and data-reduction procedures for the 18-hole probe.

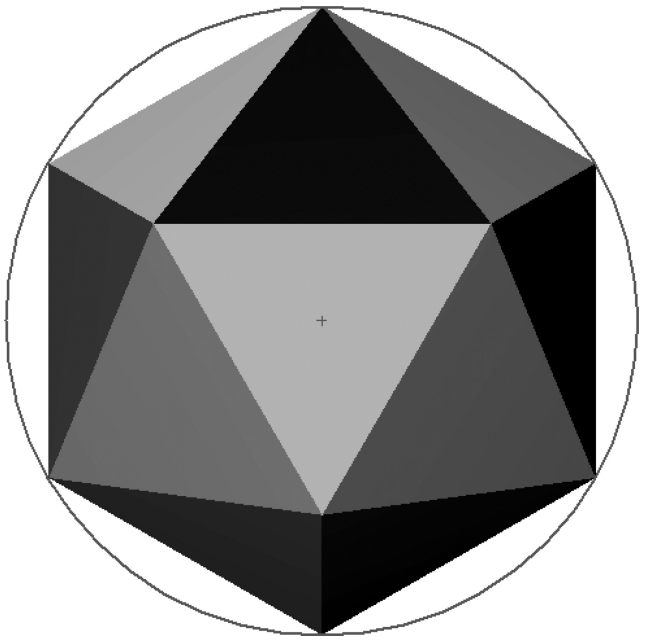

Fig. 2 Icosahedron inscribed inside a sphere; ports of 12-hole probe are located at 12 apexes of the icosahedron.

Basic Principle of the Algorithm

At any measurement point in the flow, the four quantities we are attempting to calculate are the two flow angles, the magnitude of the flow velocity U (or total pressure P_t), and the static pressure P_s. The flow angles are the angles that fully define the orientation of the local flow velocity vector with respect to the probe coordinate system $x_p y_p z_p$. These angles are the cone and roll angles Θ and Φ, as defined in Fig. 3. The other two angles defined in Fig. 3, that is, the pitch and yaw angles α and β, can alternatively be used to describe the orientation of the velocity vector. Angles α and β can be expressed in terms of angles Θ and Φ, and vice versa. The probe coordinate system, which will be referred to as the global coordinate system, is defined as follows: Axis x_p is along the probe axis, from the tip to the probe base, whereas plane $x_p y_p$ is defined by a reference surface, which is one of the six flat surfaces of a hexagonal sleeve mounted at the back of the probe.

Let us consider four ports on the surface of the tip (taken as a sphere here) at arbitrary locations, as shown in Fig. 4. The ports are represented by the circles. As will be discussed later, the locations of the ports cannot be totally arbitrary, and there are some restrictions regarding their relative position to ensure that the four pressures measured by the ports can yield accurate estimates of the flow quantities of interest. With the probe positioned at a point in the flowfield it intends to measure, let the stagnation point (SP) be on the tip surface represented by the star in Fig. 4. The center of the sphere is point C (not shown in Fig. 4). Without loss of generality, let each port be numbered according to the magnitude of the pressure it senses, that is, port 1 measures the highest pressure and port 4 the lowest. The direction of the flow velocity vector is defined by SP-C. Because the positions of the four ports are fixed and known in

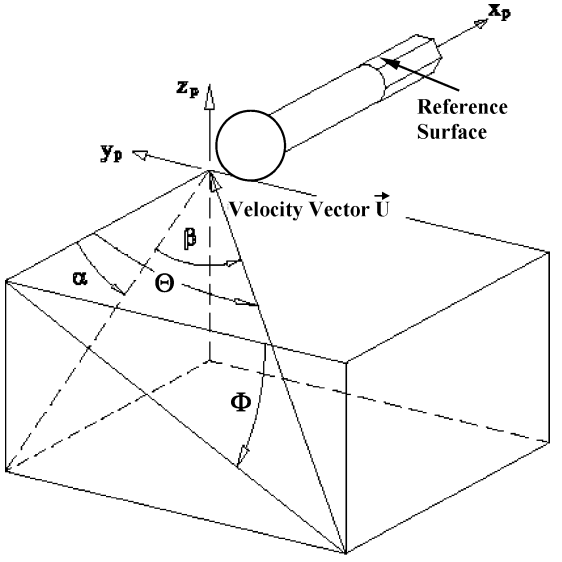

Fig. 3 Global coordinate system for probe.

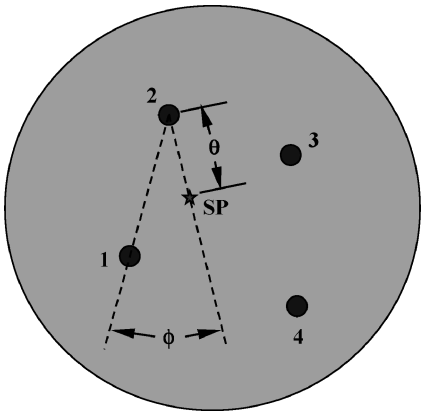

Fig. 4 Local coordinate system for probe.

the global coordinate system, the problem of finding the flow angles reduces to finding the location of SP in the local coordinate system, in terms of the angles θ and ϕ, as defined in Fig. 4. Angle θ is the angle between lines C-SP and C-2, whereas angle ϕ is the angle between planes C-2-1 and C-2-SP.

The pressures at the four ports can be written as

$$P_i = P_s + q \cdot Cp_i \tag{1}$$

where P_s is the static (freestream) pressure, q is the dynamic pressure $(1/2)\rho U^2$, and Cp_i is the pressure coefficient at port i, $i = 1, 2, 3, 4$. For the sake of illustration, we assume potential flow with the surface velocity distribution give as

$$u_i = (3/2) \cdot U \cdot \sin(\psi_i) \tag{2}$$

where angle ψ_i describes the position of port i with respect to SP and is the angle between lines C-SP and $C - i$, where $i = 1, 2, 3, 4$. Then, Eq. (1) can be written as

$$P_i(\psi_i, U, P_s) = P_s + (1/2) \cdot \rho \cdot U^2\left[\left(9/4\right)\cos^2(\psi_i) - (5/4)\right] \tag{3}$$

Because the geometric location of port i on the sphere is known, by applying simple geometric analysis we can easily show that the angle ψ_i is simply a function of the two unknown angles θ and ϕ, that is, $\psi_i = \psi_i(\theta, \phi)$. For example, in reference to Fig. 4, if (θ_3, ϕ_3) represent the coordinates of port 3 in the local coordinate system, then

$$\psi_3(\theta, \phi) = 2 \cdot \sin^{-1}\sqrt{[1 - \cos\theta_3 \cdot \cos\theta - \sin\theta_3 \cdot \sin\theta \cdot \cos(\phi_3 - \phi)]/2} \tag{4}$$

Thus, Eq. (3) can be written as

$$P_i(\theta, \phi, U, P_s) = P_s + (1/2) \cdot \rho \cdot U^2\{(9/4)\cos^2[\psi_i(\theta, \phi)] - (5/4)\} \tag{5}$$

We now have four equations [Eq. (5), for i from 1 to 4], and four unknowns, θ, ϕ, U, and P_s, and can, therefore, solve for all four unknowns. We come to the same conclusion even if we relax our assumption of potential flow and consider laminar viscous flow with a surface-velocity distribution given by White[21]:

$$u_i = U\left(1.5 \cdot \psi_i - 0.4371 \cdot \psi_i^3 + 0.1481 \cdot \psi_i^5 - 0.0423 \cdot \psi_i^7\right) \tag{6}$$

These steps illustrate the basic principle of the algorithm. A few comments are in order here to ensure that the preceding equations can be uniquely solved for the flow unknowns. If we are to determine all four flow quantities, θ, ϕ, U, and P_s, it is very important that all four ports are in the attached flow region. If only n ports are in the attached region ($n < 4$), then only n out of the four unknowns can be determined. Moreover, for certain port arrangements, the possibility exists that there may be a stagnation point for which all angles ψ_i are equal, in which case not all four equations are independent of each other, and, therefore, not all four unknowns can be determined. Also, if three of the four ports on the surface of the sphere are roughly collinear, that is, if the three lines C-i, with i corresponding to the three ports, are on the same plane, the algorithm's prediction is found to deteriorate.

If the probe tip were a perfect sphere, and the port locations were accurately known, there would be no need for experimental calibration of the probe. The preceding theoretical analysis would be enough to yield, from the four measured port pressures (as long as all four ports are in the attached flow region), reasonably accurate answers for the flow velocity, angularity, and static pressure. However, this is typically not the case. The probe tip is not a perfect sphere, and probe machining imperfections (especially for small probe tip diameters) make it practically impossible to know exactly the port locations. This necessitate probe calibration.

Design of Nondimensional Pressure Coefficients

One of the challenges when working with a generic port arrangement, not necessarily resembling the conventional five- or seven-hole port arrangement pattern, is that the conventional definition of the nondimensional pressure coefficients either can no longer be applied, or, if it can be applied, it may be far from optimal. The preceding statement is explained hereafter.

Note that, in addition to sensitivity, two important properties of a properly defined coefficient are 1) independence from the other three variables[14] (for example, that the yaw angle coefficient be independent of the pitch angle and the dynamic and static pressures and 2) smooth, and preferably linear, behavior.

Our experience with multihole probes has repeatedly demonstrated that a smooth and linear coefficient behavior is quite important for increased data-reduction accuracy.[5] Consider the two port arrangement patterns in Fig. 5. Figure 5a shows a typical five-hole port arrangement, whereas Fig. 5b shows a nonconventional port arrangement. For the five-hole arrangement, for high-angle flow, when, for example, ports 2, 1, and 4 sense the highest, second-highest, and third-highest pressures, respectively, the roll angle coefficient is typically defined as

$$C_\phi = \frac{P_2 - P_4}{q_{\text{est}}} = \frac{P_2 - P_4}{P_1 - (P_2 + P_4)/2} \tag{7}$$

which is intuitive and exhibits both of the properties stated earlier to an acceptable degree (although the technique proposed here significantly improves the behavior of the pressure coefficients for conventional probes as well). However, for the nonconventional pattern of Fig. 5b, there is no obvious way to define a roll angle coefficient properly. (Ports 1–4 sense pressures from the highest to the lowest, in order.) Even if one stretched the boundaries of intuition and defined the coefficient as

$$C_\phi = \frac{P_3 - P_4}{q_{\text{est}}} = \frac{P_3 - P_4}{P_1 - (P_2 + P_3 + P_4)/3} \tag{8}$$

one would soon find that this coefficient does not have the desired properties we discussed earlier. For the purposes of design, theoretical pressure data for the 18-hole probe were generated based on Eq. (6) (laminar viscous flow over a sphere). Figure 6 shows the roll angle coefficient, defined as in Eq. (8), for a typical sector in the 18-hole probe. As seen in Fig. 6, the coefficient exhibits strong nonlinearity. Furthermore, the q_{est} defined in the denominator in Eq. (8), which is supposed to be an estimate of the dynamic pressure and should, thus, be fairly constant for a fixed velocity magnitude and static pressure, regardless of flow angle, does not have the desired

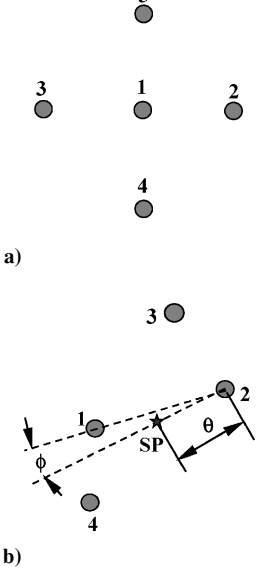

Fig. 5 Port arrangement: a) conventional arrangement and b) generic/nonconventional arrangement.

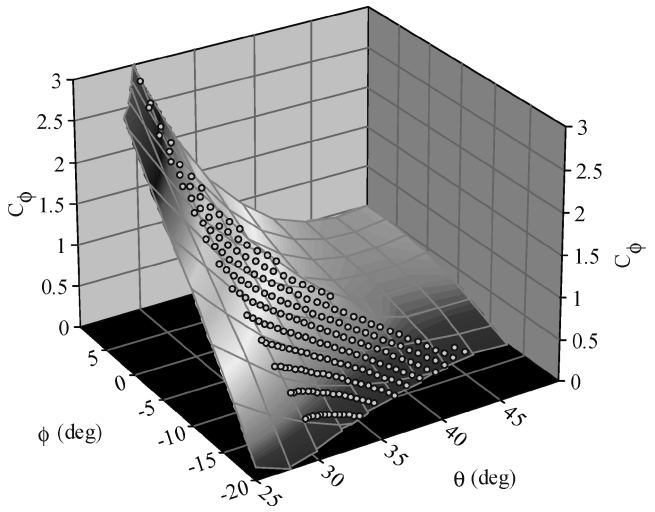

Fig. 6 Roll angle coefficient defined conventionally in sample sector of 18-hole probe.

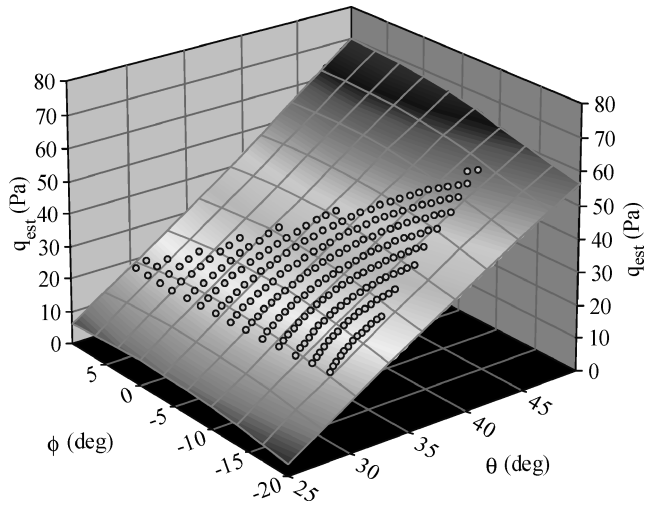

Fig. 7 Estimated dynamic pressure defined conventionally in sample sector of 18-hole probe.

near-constant value, as shown in Fig. 7. The actual dynamic pressure for all of the points in Fig. 7 is a constant equal to 61.25 Pa.

Moreover, the way we went about defining the coefficient is heuristic, and the definition is quite likely to change as the port pattern changes. This preceding discussion makes it obvious that a procedure is needed through which, for any nonconventional port arrangement, we can design the coefficients methodically such that they exhibit the desired properties. This procedure is described next.

Consider a multihole probe with a nonconventional port arrangement (such as the 18-hole or the 12-hole probe). First, the ports are numbered for identification of their location on the tip. The specific numbering scheme is not important, as long as it identifies the location of a port on the tip. Let us now assume that, for a specific flow condition, the three ports that sense the highest pressures, in order of decreasing magnitude, have the numbers max1, max2, and max3, respectively. In the Θ–Φ domain (definitions of Θ and Φ in Fig. 3), we define sectors pertaining to ports max1–max3 as follows:

$$\text{Sector number} = \max 1 \times 10^4 + \max 2 \times 10^2 + \max 3$$

As an example, Fig. 8 presents a schematic of the sector arrangement in the case where max1, max2, and max3 take values from 1 to 5. In Fig. 8, each sector is the locus of all possible stagnation points (in the Θ–Φ domain) that result in the order of the three highest pressures indicated by the number of the sector. For example, the triangle labeled 20103 is the locus of all possible stagnation points that result in port 2 sensing the highest pressure and ports 1 and 3 sensing the second- and third-highest pressures, respectively. Each sector is only schematically represented as a triangle for simplicity. In reality, its boundaries are not necessarily straight lines. A local coordinate system is assigned to each sector as shown in Fig. 9 (same as that of Fig. 4).

For each sector, the following procedure is followed in designing the coefficients. Let us consider sector 10203. For each stagnation point in the sector, the port with the fourth-highest pressure is identified. The port with the most occurrences of the fourth-highest pressure is labeled max4 for that sector. For example, for sector 10203, max4 = 4, for sector 30102, max4 = 5. Then, for all points in the sector (from the calibration database), the following linear surfaces/fits are generated:

$$\Delta P1/q = (P_{\max 1} - P_{\max 3})/q = a1 + b1 \cdot \theta + c1 \cdot \phi \quad (9)$$

$$\Delta P2/q = (P_{\max 2} - P_{\max 3})/q = a2 + b2 \cdot \theta + c2 \cdot \phi \quad (10)$$

$$\Delta P3/q = (P_{\max 3} - P_{\max 4})/q = a3 + b3 \cdot \theta + c3 \cdot \phi \quad (11)$$

where θ and ϕ are the local stagnation point coordinates in radians, and $a1$, $b1$, $c1$, $a2$, $b2$, $c2$, $a3$, $b3$, and $c3$ are (nondimensional) constants determined by the least-squares fitting. The numerator contains the difference of pressures to eliminate dependence on the static pressure P_s and is divided by the dynamic pressure q to eliminate dependence on q. It turns out that, for the 18-hole probe at least, these linear fits have very high correlation coefficients (R^2 value), equal to or higher than 0.95. Subsequently, Eqs. (9) and (10) are solved for θ and ϕ:

$$\theta = \theta_0 + A_\theta \cdot (\Delta P1/q) + B_\theta \cdot (\Delta P2/q) \quad (12)$$

$$\phi = \phi_0 + A_\phi \cdot (\Delta P1/q) + B_\phi \cdot (\Delta P2/q) \quad (13)$$

where the constants A_θ, B_θ, A_ϕ, and B_ϕ are found by inverse transformation of Eqs. (9) and (10). In Eqs. (12) and (13), note that θ_0 and ϕ_0 are the coordinates (in radians) of the stagnation point for which $P_{\max 1} = P_{\max 2} = P_{\max 3}$. Then, the flow angle nondimensional pressure coefficients C_θ and C_ϕ are defined as

$$C_\theta = \theta - \theta_0 = (A_\theta \cdot \Delta P1 + B_\theta \cdot \Delta P2)/q \quad (14)$$

$$C_\phi = \phi - \phi_o = (A_\phi \cdot \Delta P1 + B_\phi \cdot \Delta P2)/q \quad (15)$$

The next challenge is to generate an estimate of the dynamic pressure that is as independent of θ and ϕ as possible. The dynamic pressure q_{est} is expressed as

$$q_{\text{est}} = R \cdot \Delta P1 + S \cdot \Delta P2 + T \cdot \Delta P3 \quad (16)$$

$$q_{\text{est}}/q = R \cdot (\Delta P1/q) + S \cdot (\Delta P2/q) + T \cdot (\Delta P3/q) \quad (17)$$

Substituting Eqs. (9–11) in Eq. (17), and then setting the coefficients of θ and ϕ equal to zero and the constant term equal to 1, we get three equations from which the constants R, S, and T can be solved for:

$$R \cdot a1 + S \cdot a2 + T \cdot a3 = 1 \quad (18)$$

$$R \cdot b1 + S \cdot b2 + T \cdot b3 = 0 \quad (19)$$

$$R \cdot c1 + S \cdot c2 + T \cdot c3 = 0 \quad (20)$$

Equations (18–20) force q_{est} to be equal to the actual q and make it independent of the variables θ and ϕ. By setting $q = q_{\text{est}}$ and substituting Eq. (16) in Eqs. (14) and (15), the coefficients C_θ and C_ϕ can be defined explicitly as

$$C_\theta = \frac{A_\theta \cdot (P_{\max 1} - P_{\max 3}) + B_\theta \cdot (P_{\max 2} - P_{\max 3})}{R \cdot (P_{\max 1} - P_{\max 3}) + S \cdot (P_{\max 2} - P_{\max 3}) + T \cdot (P_{\max 3} - P_{\max 4})} \quad (21)$$

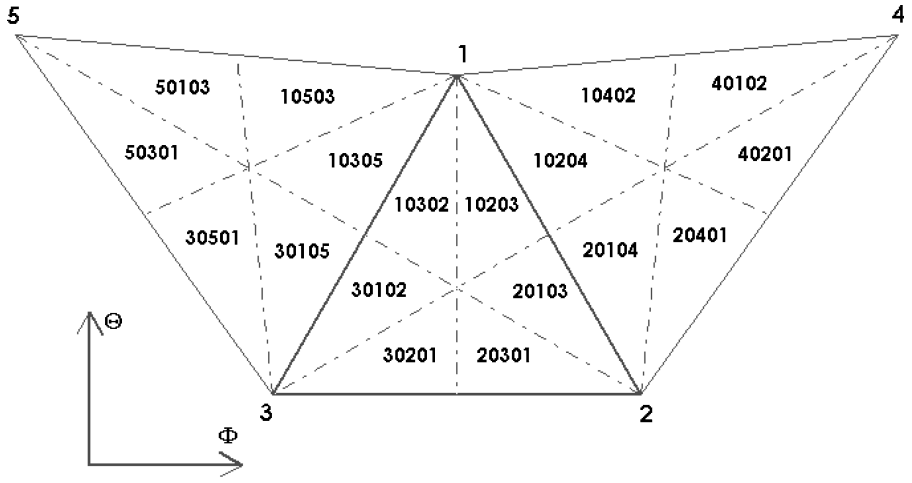

Fig. 8 Sector arrangement.

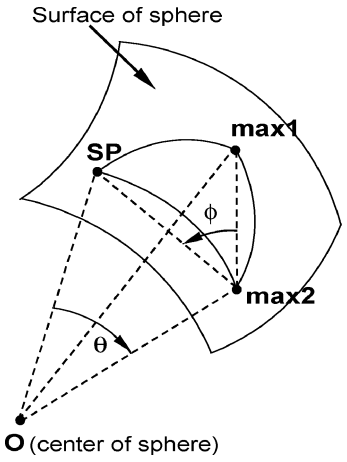

Fig. 9 Local coordinate reference system.

$$C_\phi = \frac{A_\phi \cdot (P_{\max 1} - P_{\max 3}) + B_\phi \cdot (P_{\max 2} - P_{\max 3})}{R \cdot (P_{\max 1} - P_{\max 3}) + S \cdot (P_{\max 2} - P_{\max 3}) + T \cdot (P_{\max 3} - P_{\max 4})} \tag{22}$$

Finally, the nondimensional coefficients C_s and C_t for the static and total pressure are defined as

$$C_s = \frac{P_{\max 1} - P_s}{q_{\text{est}}} = \frac{P_{\max 1} - P_s}{R \cdot \left(P_{\max 1} - P_{\max 3}\right) + S \cdot (P_{\max 2} - P_{\max 3}) + T \cdot (P_{\max 3} - P_{\max 4})} \tag{23}$$

$$C_t = \frac{P_{\max 1} - P_t}{q_{\text{est}}} = \frac{P_{\max 1} - P_t}{R \cdot (P_{\max 1} - P_{\max 3}) + S \cdot (P_{\max 2} - P_{\max 3}) + T \cdot (P_{\max 3} - P_{\max 4})} \tag{24}$$

The C_s and C_t definitions can be used irrespective of their dependence on flow angles, as long as they are velocity-invariant and well-behaved surfaces as functions of θ and ϕ. Note that the numerators in Eqs. (23) and (24) are identical to those in traditional definitions of C_s and C_t.

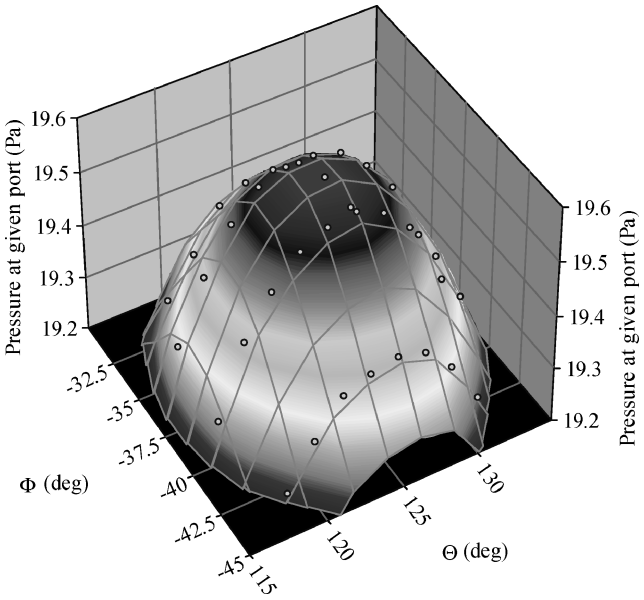

Fig. 10 Pressure at port 2 of an 18-hole probe, varying with the stagnation point location or, equivalently, flow angles.

Probe Calibration

The pressure data required for checking the designed coefficients can be either theoretically or experimentally generated. However, if the data used are theoretically generated, the quality of the designed coefficients will have to be ultimately tested with the experimental/calibration data. Both theoretical data and experimental data (obtained via probe calibration) were used to validate the quality of the designed coefficients.

A typical 18-hole probe with a tip diameter of 0.25 in. was fabricated (Fig. 1) and calibrated in a high-speed wind tunnel at different Mach numbers: 0.05, 0.1, 0.2, 0.3, 0.4, 0.5, 0.6, and 0.7. The experimentally obtained calibration database for the 18-hole probe consists of all 18 port pressures and the freestream dynamic pressure for a wide range of flow angles. The cone angle Θ was varied from 0 to about 150 deg in steps of 1.8 deg. For each one of these cone angles, the roll angle Φ was varied from -180 to 180 deg in steps of 3.6 deg. Thus, a total of about 8000 calibration points (SP locations) all around the probe tip (except near the sting) are available. The probe was mounted on a two-axis stepper-motor assembly, which can vary the cone and roll angles Θ and Φ through the desired range just stated. Note that the design of the assembly is such that, regardless of the probe orientation, the center of the spherical probe tip always stays at the same point. At each of the probe orientations the

19 pressures were acquired with a 32-transducer electronic pressure scanner (ESP) from PSI, Inc. An ESP unit with a pressure range of ± 10 in. H_2O (2.49 kPa) was used for the $M = 0.05$ and the $M = 0.1$ calibrations, a ± 20 in. H_2O (4.98 kPa) unit was used for the $M = 0.2$ calibration, and a ± 10 psi (68.95 kPa) unit was used for all of the other calibrations. At each probe orientation, 2 s were allowed for the flow to settle, and then measurements were taken for 4 s at 256 Hz with a 12-bit data acquisition board. The uncertainty in the probe positioning is negligible and is of the order of 0.001 deg. All ESP units used were calibrated before each calibration. This yielded a pressure measurement uncertainty of 0.08% full-scale output (FSO) for each ESP unit. The wind-tunnel generates a jet out of a nozzle, 1 in. $\times$ 2 in. (2.5 cm $\times$ 5 cm) in dimension, and can attain a maximum speed of 320 m/s with a freestream turbulence of less than 0.25%.

Preprocessing Calibration Data

First, the data in the calibration database are allocated among all of the sectors and transformed into the respective local coordinate systems. Then the coefficients A_θ, B_θ, A_ϕ, B_ϕ, R, S, and T for each of the sectors, as described in the preceding sections, are calculated. Only those sectors with at least five calibration points within them are chosen as valid. The points lying in any of the discarded sectors are reassigned to adjacent sectors. Also, if the highest three pressure ports are found to be collinear as described earlier, $\Delta P3$ in Eq. (11) can be redefined as $(P_{\max 2} - P_{\max 4})$ and was found to work well. Alternatively, the third-highest pressure port could be discarded and another port in the attached flow region (if available) can be selected. The second technique was used for the 18-hole probe because there was always an extra port available. Then, for each calibration point, the nondimensional coefficients, C_θ, C_ϕ, C_s and C_t, and the stagnation point coordinates (θ, ϕ) in the local reference system, as described in Fig. 9, are calculated. To calculate the latter, it is necessary to have at least a rough estimate of the coordinate locations of the pressure ports. Because of the inevitable deviation from the design port location while machining, these have to be estimated based on the pressures from the calibration database. The pressure at any port due to the nearest few stagnation points behaves as shown in Fig. 10. When a second-order surface is fit through the points and the (Θ, Φ) corresponding to the local maximum is found, a good estimate of the port's coordinate location can be obtained.

Quality Validation of Defined Pressure Coefficients

As an example, sector 10205 of the 18-hole is chosen to illustrate the behavior of the nondimensional coefficients designed here. Based on theoretically generated pressure data, for this sector, the constants A_θ, B_θ, A_ϕ, B_ϕ, R, S, and T are found to be 0.330, -0.272, -0.450, -0.658, 1.074, 1.128, and 1.037, respectively. The port pressures (hence, $P_{\max 1}$, $P_{\max 2}$, etc.) and P_s and P_t (flow conditions) at different (θ, ϕ) locations within the sector are known. Hence, the four coefficients in Eqs. (21–24) and also q_{est} in Eq. (16) can be plotted for the sector as functions of the local θ and ϕ. Figures 11a and 12a present plots of $C_\theta(\theta, \phi)$ and $C_\phi(\theta, \phi)$, respectively, based on theoretical data. Very good behavior is observed.

To show that the designed coefficients behave equally well when applied to the actual (experimentally generated) calibration data, Figs. 11b and 12b present plots of $C_\theta(\theta, \phi)$ and $C_\phi(\theta, \phi)$,

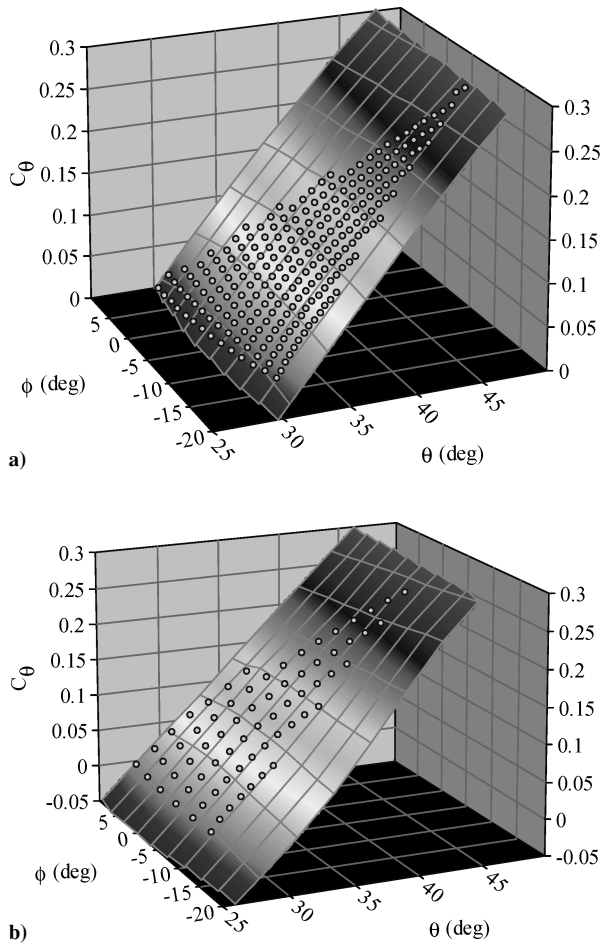

Fig. 11 Typical behavior of newly defined cone angle coefficient [Eq. (21)] for 18-hole probe: a) theoretical data and b) probe calibration data.

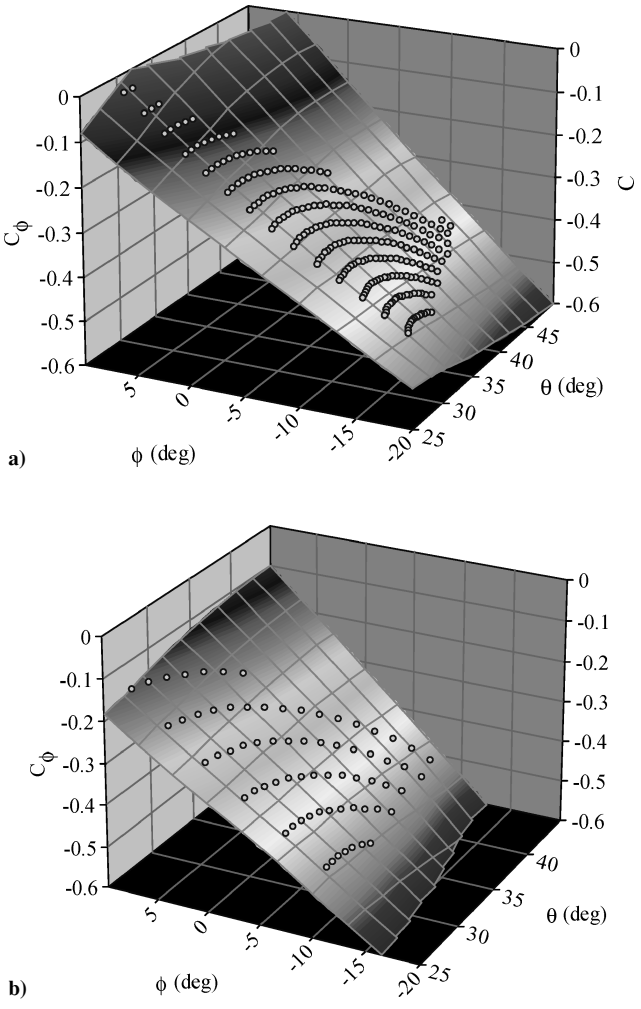

Fig. 12 Typical behavior of newly defined roll angle coefficient [Eq. (22)] for 18-hole probe: a) theoretical data and b) probe calibration data.

respectively, for the same sector, with experimental calibration data. For this case, and using the experimental calibration data, the constants A_θ, B_θ, A_ϕ, B_ϕ, R, S, and T were found to be 0.361, −0.390, −0.595, −0.513, 1.176, 0.996, and 1.146, respectively (vs 0.330, −0.272, −0.450, −0.658, 1.074, 1.128, and 1.037, for the theoretically generated data). It is clear that the experimental surfaces have the desired qualities/properties and behave similar to the theoretical data. Note here that the viscous sphere pressure distribution equation (6) is used only with the intention of studying the newly designed non-dimensional probe coefficients. For the actual probe calibration and reduction, the pressure data are obtained experimentally and used exclusively, as explained in the next sections. As seen in Figs. 11 and 12, both for theoretical and experimental data, and contrary to the behavior of the conventional coefficient definition represented in Fig. 6, it is clear that $C_\theta(\theta, \phi)$ demonstrates smooth and linear behavior and good independence from ϕ, whereas $C_\phi(\theta, \phi)$ demonstrates smooth and linear behavior and good independence from θ. As explained earlier, both C_θ and C_ϕ are designed to be independent of P_s and q. This means that the calibration data obtained at some flow conditions (P_s, q) can be used for all flow conditions (within a reasonable Mach number range, typically of ± 0.1).

Figure 13 presents $q_{\text{est}}(\theta, \phi)$ obtained with theoretical pressure data. The actual dynamic pressure for all of the points here is, as before, 61.25 Pa. It is clear that $q_{\text{est}}(\theta, \phi)$ demonstrates smooth and nearly constant behavior (especially as compared to that of Fig. 7) and independence from θ and ϕ. Figures 14 and 15 present C_s and C_t, respectively (again, with theoretical data), illustrating well-behaved surfaces.

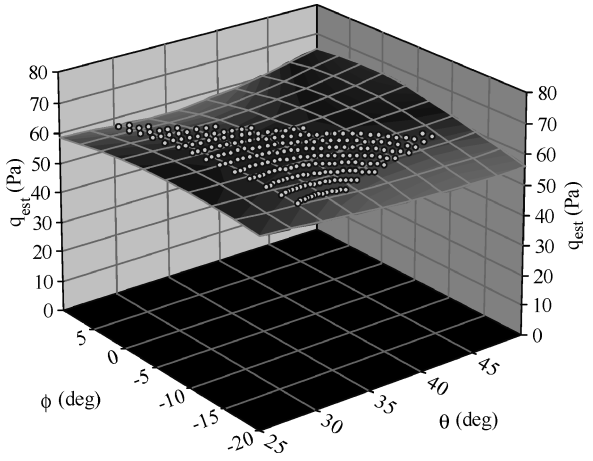

Fig. 13 Typical behavior of newly defined estimated dynamic pressure [Eq. (16)].

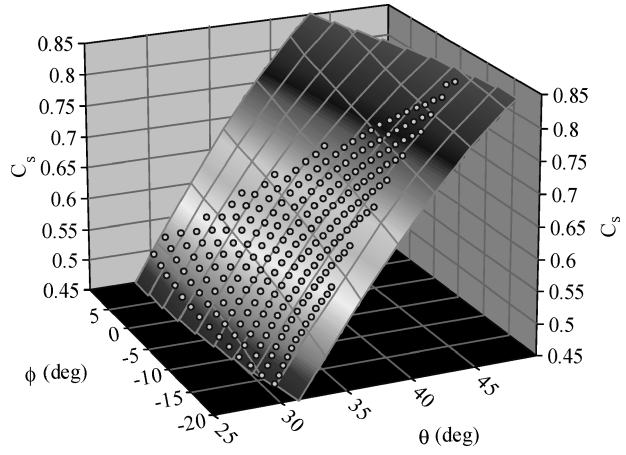

Fig. 14 Typical behavior of newly defined static pressure coefficient [Eq. (23)].

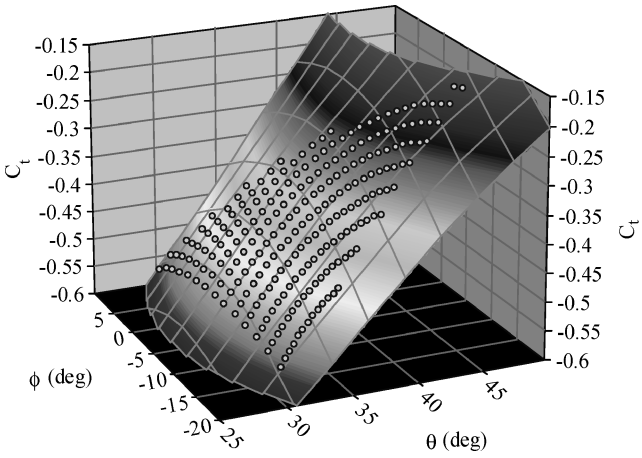

Fig. 15 Typical behavior of newly defined total pressure coefficient [Eq. (24)].

Data Reduction

During an actual application of the probe, the following procedure is followed to calculate the flow variables: the two flow angles, the static pressure, and the total pressure. For a given measurement data point, all port pressures are measured. Based on the highest three pressures, the sector number and the corresponding coefficients for the sector are obtained. At this point, the algorithm checks whether the sector number obtained is valid, that is, whether the sector is existent. If the sector number is found as one that was removed during preprocessing due to insufficient number of points within it, then the current test point is assigned to a suitable adjacent sector. Recall that, during the coefficient designing procedure, we generated seven coefficients, A_θ, B_θ, A_ϕ, B_ϕ, R, S, and T, for each sector, that are used in defining the nondimensional coefficients C_θ and C_ϕ and the estimated dynamic pressure q_{est}. Using these coefficients, C_θ and C_ϕ are calculated for the data point. $C_{\theta-\text{cal}}$ and $C_{\phi-\text{cal}}$ for the adjacent calibration points are obtained from the preprocessed calibration database. From these, the closest 30 calibration points are selected, based on their Euclidean distance d from the current (C_θ, C_ϕ):

$$d = \sqrt{(C_\theta - C_{\theta-\text{cal}})^2 + [\lambda \cdot (C_\phi - C_{\phi-\text{cal}})]^2} \tag{25}$$

The scaling factor λ is introduced in Eq. (25) to bring both of the coefficients to the same scale and is defined for every sector based on the maximum and minimum values of its coefficients[15]:

$$\lambda = \frac{(C_\theta)_{\max} - (C_\theta)_{\min}}{(C_\phi)_{\max} - (C_\phi)_{\min}} \tag{26}$$

To deal properly with data points that might be very close to the boundaries of a sector, calibration points from 10 adjacent sectors are also considered. For example, if the data point is in sector 10203 (Fig. 8), calibration points from sectors 10204, 20103, 10302, and so on are also used. The selected points are distributed into four quadrants in the C_θ–C_ϕ plane with the data point's (C_θ, C_ϕ) as the origin. This is done to ensure that the selected calibration points enclose the test point. Out of the points thus distributed, the nearest one from each quadrant is selected, one quadrant after the other, until the required number of calibration points m is obtained. Least-squares surface fits are performed locally on the selected calibration points for each of the four variables. Subsequently, these fits are used to calculate the quantities θ, ϕ, C_s, and C_t corresponding to the current data point (C_θ, C_ϕ). A quadratic fit with $m = 8$ is seen to produce the best results. The θ and ϕ calculated are converted to global coordinates to get the global flow angles Θ and Φ. Then, the static and total pressures (P_s and P_t) are calculated from

$$P_s = P_{\max 1} - C_s \cdot q_{\text{est}} \tag{27}$$

$$P_t = P_{\max 1} - C_t \cdot q_{\text{est}} \tag{28}$$

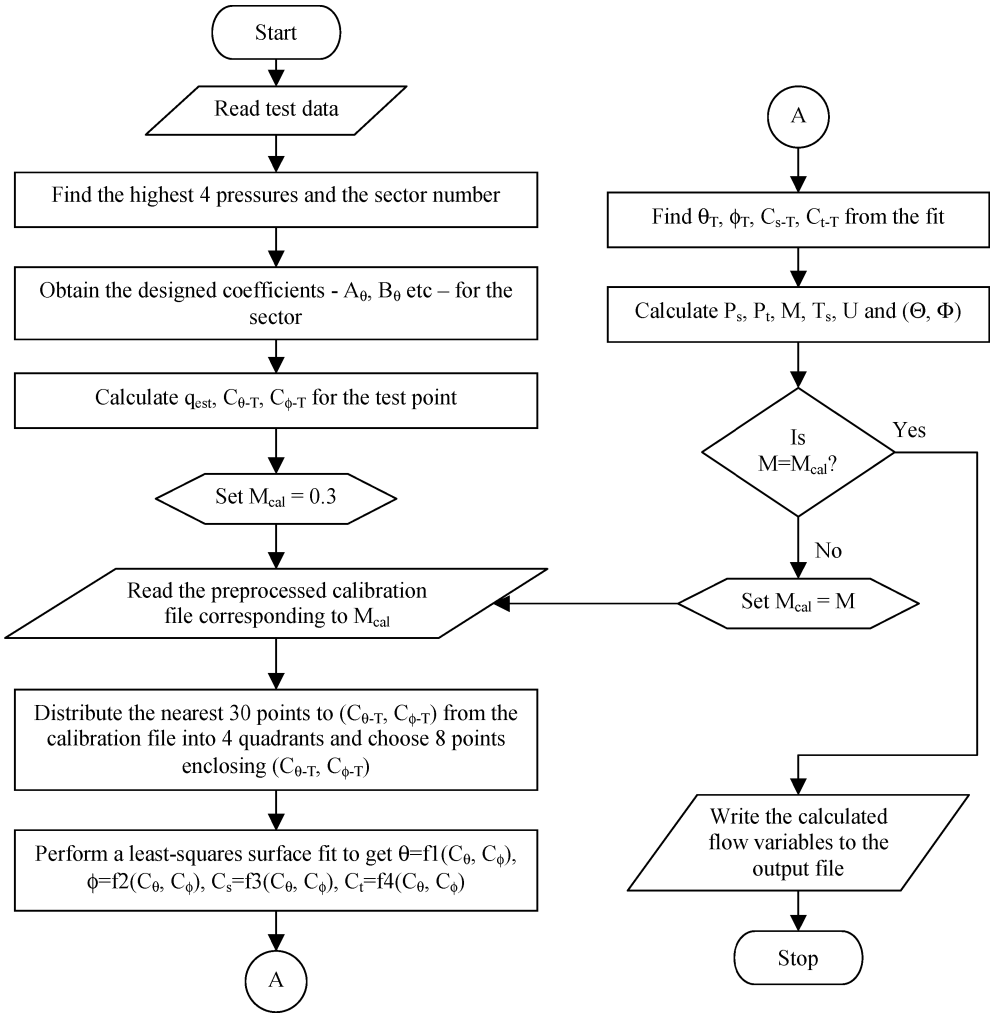

Fig. 16 Data-reduction process.

When isentropic, perfect-gas relationships are used for air, the Mach number M and static temperature T_s are calculated:

$$M = \sqrt{5\left[(P_t/P_s)^{\frac{2}{7}} - 1\right]} \tag{29}$$

$$T_s = T_t/(1 + M^2/5) \tag{30}$$

The freestream velocity magnitude is then arrived at by the equation

$$U = M \cdot \sqrt{\gamma \cdot R \cdot T_s} \tag{31}$$

Finally, the velocity components in the probe (global) coordinate system are calculated:

$$U_x = U \cdot \cos\Theta, \qquad U_y = U \cdot \sin\Theta \cdot \cos\Phi$$

$$U_z = U \cdot \sin\Theta \cdot \sin\Phi$$

The flowchart in Fig. 16 illustrates the entire data-reduction process.

To account for Mach number effects, a probe is typically calibrated in a range of Mach numbers, in steps of 0.1 in the Mach number (for example, at Mach 0.1, 0.2, 0.3, etc.), thus generating several calibration files/databases, one per Mach number. When the probe is used in an unknown flowfield, as the Mach number at the measurement location is not known, it is unknown which calibration file/database to use for the data reduction of the specific point. Therefore, because during data reduction it is necessary to arrive at the correct calibration file that corresponds to the flow Mach number, an iterative scheme is adopted. If the calibration file used for data reduction corresponds to a Mach number quite different from that of the measurement point, the predicted results can be erroneous. For example, the percentage error in the velocity magnitude for a flow at Mach 0.2 reduced with calibration data from Mach 0.5 was found to be as much as 6%. Although this is high, it serves to obtain a very good initial estimate of the measurement point's Mach number (0.2 in this case). Therefore, for the first iteration, one can reduce the test data with, for example, the Mach 0.3 calibration database and estimate the Mach number of the flow. Then a second iteration can be performed with the calibration database nearest to this estimated Mach number. We have implemented this procedure with conventional multihole probes with very good results.[15]

Results and Discussion

The algorithm was coded in MATLAB® 6.1 and, in its present state, can reduce 250 points per second (in a 512-MB RAM, 2.4-GHz Pentium-IV computer). The reduction code was tested with the calibration data for the 18-hole probe. The calibration data themselves were used as test data. It was made certain that, for every test point, its own data were removed from the calibration data during reduction. The data consisted of 7400 test points obtained at a Mach number of 0.2, with the Θ coordinate ranging up to 145 deg. Very accurate predictions were attained for the flow angles, the velocity magnitude, and the static and total pressures. Figures 17 and 18 present the individual error histograms for the flow angles in the global reference system (Θ and Φ). Figure 19 shows the histogram of the error (in percent) for the freestream velocity magnitude U. The percent errors, taken with respect to the freestream dynamic pressure q, in the predicted static and total pressures P_s and P_t,

Table 1 Error data for predicted variables at $M = 0.2$ with probe calibration data

Error	Maximum	Mean μ	Standard deviation σ
Error in Θ, deg	0.444	0.002	0.061
Error in Φ, deg	0.946	−0.004	0.122
Error% in U	0.654	−0.008	0.086
Error% in P_s with respect to q	1.127	0.024	0.128
Error% in P_t with respect to q	0.713	0.008	0.096

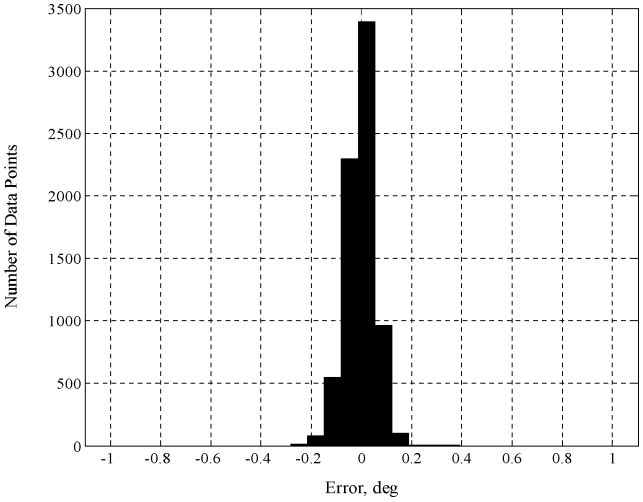

Fig. 17 Histogram of error in predicted cone angle Θ in degrees.

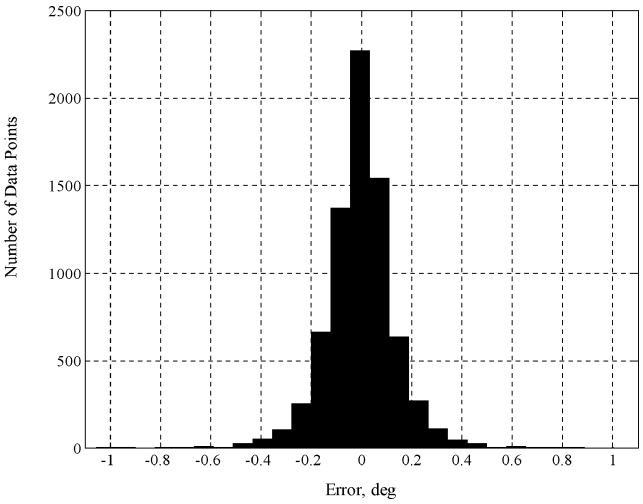

Fig. 18 Histogram of error in predicted roll angle Φ in degrees.

are shown in Figs. 20 and 21. In all of these plots (Figs. 17–21), Gaussian error distributions are observed, with means very close to zero, which shows that there were no bias errors in the calibration or data-reduction processes.

Table 1 shows the statistical data from the error analysis. Note that these results were obtained with a handicap, that is, for every test point, the test point itself was not part of the calibration points used for data reduction. This results in larger Euclidean distances between the test point and the nearest calibration points, as compared to the case in which the test points are at intermediate locations. Yet, very good predictions are observed as seen from the small standard deviations. For example, for the error in Θ (Table 1), a standard deviation of 0.061 deg means that about 68% of the predictions will have an error (compared to the exact Θ angle) less than or equal to

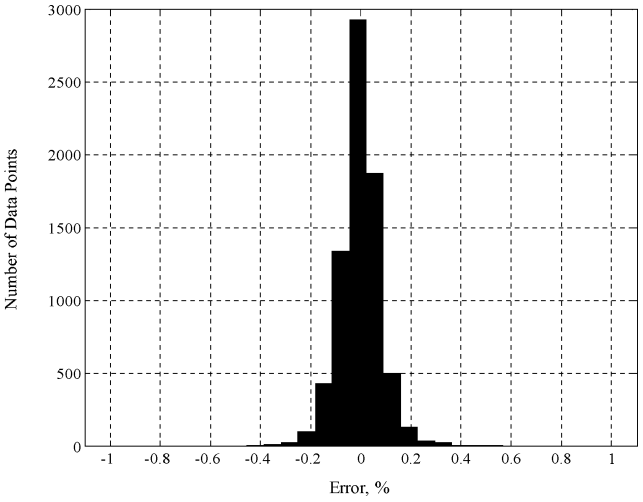

Fig. 19 Histogram of percentage error in predicted velocity magnitude U.

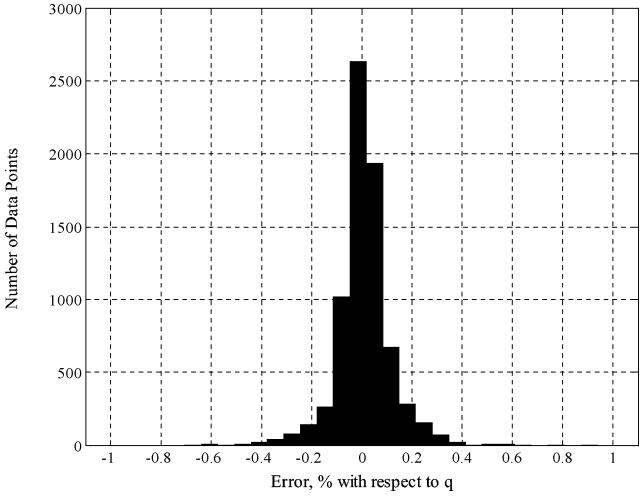

Fig. 20 Histogram of error in predicted static pressure P_s as percentage of dynamic pressure q.

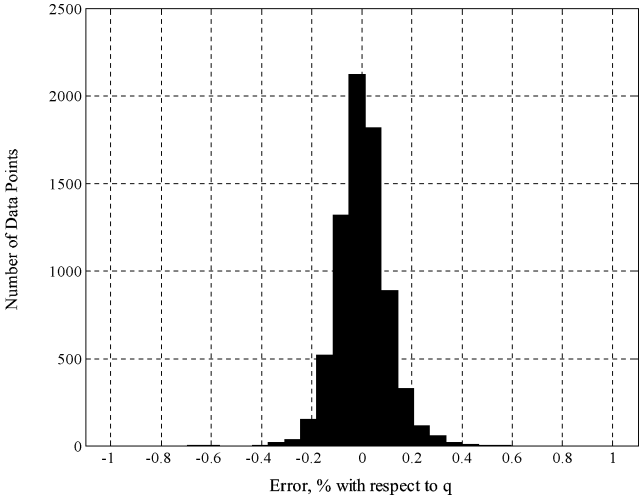

Fig. 21 Histogram of error in predicted total pressure P_t as percentage of dynamic pressure q.

Table 2 Error data for predicted variables at $M = 0.05$ with probe calibration data

Error	Maximum	Mean μ	Standard deviation σ
Error in Θ, deg	0.548	0.001	0.081
Error in Φ, deg	1.324	−0.004	0.162
Error% in U	0.615	−0.010	0.130
Error% in P_s with respect to q	1.392	0.024	0.150
Error% in P_t with respect to q	1.024	0.004	0.201

Table 3 Error data for predicted variables at $M = 0.7$ with probe calibration data

Error	Maximum	Mean μ	Standard deviation σ
Error in Θ, deg	0.598	0.001	0.061
Error in Φ, deg	1.210	0.001	0.131
Error% in U	1.311	−0.002	0.130
Error% in P_s with respect to q	1.706	0.013	0.188
Error% in P_t with respect to q	1.054	0.012	0.097

Table 4 Error data for predicted variables at $M = 0.2$ with sector coefficients from $M = 0.7$ (probe calibration data)

Error	Maximum	Mean μ	Standard deviation σ
Error in Θ, deg	0.423	−0.003	0.059
Error in Φ, deg	1.136	−0.005	0.135
Error% in U	0.512	−0.002	0.081
Error% in P_s with respect to q	0.870	0.013	0.111
Error% in P_t with respect to q	0.631	0.010	0.102

Table 5 Error data for predicted variables at $M = 0.2$ with theoretical pressure data

Error	Maximum	Mean μ	Standard deviation σ
Error in Θ, deg	0.081	0.000	0.005
Error in Φ, deg	0.085	0.000	0.006
Error% in U	0.112	0.000	0.006
Error% in P_s with respect to q	0.075	0.000	0.005
Error% in P_t with respect to q	0.172	0.001	0.009

0.061 deg, or that about 95% of the predictions will have an error less than or equal to 2×0.061 deg $= 0.122$ deg.

To check for consistency, the reduction was performed for the same probe at Mach numbers of 0.05, 0.1, 0.3, 0.4, 0.5, 0.6, and 0.7. For each case, the coefficients were designed specifically for that Mach number from their respective calibration data. In all of these cases, the means and standard deviations are found to be very similar to the Mach 0.2 case. Tables 2 and 3 show the error data at the extremes, that is, at Mach 0.05 and 0.7, respectively. The higher maximum errors in the Mach 0.7 case are due to some stray bad points and are reflective of the quality of the calibration data (rather than the algorithm's uncertainty).

Because the sector coefficients A_θ, B_θ, A_ϕ, B_ϕ, R, S, and T were designed to be independent of the freestream dynamic pressure, a test was performed in which these coefficients obtained from the pressure data at one Mach number were applied to the reduction at another Mach number. Table 4 shows the results obtained by using the sector coefficients at Mach 0.7 in calculating the flow variables at Mach 0.2. As expected, the error data behave similarly to those in Table 1.

Method's Uncertainty

The prediction error results presented in the preceding section contain the contribution to the error from the pressure measurement uncertainty of the experimental probe calibration process. To evaluate the uncertainty of the reduction process itself, the method/data reduction was applied to pressure data generated theoretically.

Table 5 shows the error data for the same conditions as the first case ($M = 0.2$ and ~8000 calibration points), but with pressure data theoretically generated using Eq. (6). The remarkably small standard deviations (and means) reveal that the source of errors is predominantly the experimental calibration procedure, rather than the reduction algorithm or the new definition of the nondimensional coefficients.

Conclusions

This work presented the development of calibration and data-reduction algorithms for nonconventional multihole pressure probes. New, generally applicable pressure coefficients were introduced that can handle nonconventional pressure port arrangements, such as that of a nearly omnidirectional 18-hole probe. The algorithms introduced herein can handle any pattern of port arrangement, from axisymmetric and regular to random. Moreover, they eliminate the need to separate the measurement domain of a probe into low-angle and high-angle regimes typical in conventional five- and seven-hole-probe algorithms that require two different sets of pressure coefficient definitions and procedures. To validate the quality of the newly defined coefficients, an 18-hole probe was fabricated and calibrated over a range of Mach numbers and flow angles. The obtained calibration data, as well as theoretically generated pressure data, were used to validate the quality of the defined coefficients. It was shown that the newly defined $C_\theta(\theta, \phi)$ demonstrates smooth and linear behavior and good independence from ϕ, whereas $C_\phi(\theta, \phi)$ demonstrates smooth and linear behavior and good independence from θ. The newly defined estimated dynamic pressure $q_{\text{est}}(\theta, \phi)$ demonstrates smooth and nearly constant behavior and independence from θ and ϕ. A data-reduction procedure was developed using the newly defined coefficients and was applied to the calibration data of the 18-hole probe. Excellent prediction capabilities are demonstrated, with standard deviations of the prediction errors on the order of 0.1 deg for the flow angles and 0.1% for the velocity magnitude. It was also shown that these errors are primarily due to the uncertainty in the measured pressures during probe calibration. The data-reduction technique itself has practically zero uncertainty.

Acknowledgment

The authors thank the Aeroprobe Corporation for providing the calibration data for the 18-hole probe.

References

[1]Bryer, D. W., and Pankhurst, R. C., *Pressure-Probe Methods for Determining Wind Speed and Flow Direction*, Her Majesty's Stationery Office, London, 1971.

[2]Everett, K. N., Gerner, A. A., and Durston, D. A., "Seven-Hole Cone Probes for High-Angle Flow Measurements: Theory and Calibration," *AIAA Journal*, Vol. 21, No. 7, 1983, pp. 992–998.

[3]Kjelgaard, S. O., "Theoretical Derivation and Calibration Technique of a Hemispherical-Tipped, Five-Hole Probe," NASA TM-4047, Sept. 1988.

[4]Zilliac, G. G., "Calibration of Seven-Hole Probes for Use in Fluid Flows with Large Angularity," NASA TM-102200, Dec. 1989.

[5]Rediniotis, O. K., Hoang, N. T., and Telionis, D. P., "The Seven-Hole Probe: Its Calibration and Use," *Forum on Instructional Fluid Dynamics Experiments*, Vol. 152, edited by R. S. Budwig, J. F. Foss, and D. E. Stock, American Society of Mechanical Engineers, New York, 1993, pp. 21–26.

[6]Kinser, R. E., and Rediniotis, O. K., "Development of a Nearly Omnidirectional Velocity Measurement Pressure Probe," *AIAA Journal*, Vol. 36, No. 10, 1998, pp. 1854–1860.

[7]Gettelman, C. C., and Krause, L. N., "Characteristics of a Wedge with Various Holder Configurations for Static-Pressure Measurements in Subsonic Gas Streams," NACA RM-E51G09, Sept. 1951.

[8]Centolanzi, F. J., "Characteristics of a 40° Cone for Measuring Mach Number, Total Pressure, and Flow Angles at Supersonic Speeds," NACA TN-3967, May 1957.

[9]Gerner, A. A., and Maurer, C. L., "Calibration of Seven-Hole Probes Suitable for High Angles in Subsonic Compressible Flows," U.S. Air Force Academy, Rept. USAFA-TR-81-4, Colorado Springs, CO, May 1981.

[10]Gerner, A. A., and Sisson, G., "Seven-Hole Probe Data Acquisition System," U.S. Air Force Academy, Rept. USAFA-TN-81-8, Colorado Springs, CO, Nov. 1981.

[11]Everett, K. N., Gerner, A. A., and Durston, D. A., "Theory and Calibration of Non-Nulling Seven-Hole Cone Probes for Use in Complex Flow Measurement," AIAA Paper 82-0232, Jan. 1982.

[12]Ostowari, C., and Wentz, W. H., "Modified Calibration Technique of a Five-Hole Probe for High Flow Angles," *Experiments in Fluids*, Vol. 1, No. 3, 1983, pp. 166–168.

[13]Houtman, E. M., and Bannink, W. J., "Calibration and Measuring Procedure of a Five-Hole Hemispherical Head Probe in Compressible Flow," Delft Univ. of Technology, Rept. LR-585, Delft, The Netherlands, April 1989.

[14]Zilliac, G. G., "Modelling, Calibration, and Error Analysis of Seven-Hole Pressure Probes," *Experiments in Fluids*, Vol. 14, No. 1/2, 1993, pp. 104–120.

[15]Johansen, E. S., Rediniotis, O. K., and Jones, G., "The Compressible Calibration of Miniature Multi-Hole Probes," *Journal of Fluids Engineering*, Vol. 123, No. 1, 2001, pp. 128–138.

[16]Rediniotis, O. K., and Vijayagopal, R., "Miniature Multihole Pressure Probes and Their Neural-Network-Based Calibration," *AIAA Journal*, Vol. 37, No. 6, 1999, pp. 666–674.

[17]Clark, E. L., Henfling, J. F., and Aeschliman, D. P., "Calibration of Hemispherical-Head Flow Angularity Probes," AIAA Paper 92-4005, July 1992.

[18]Takahashi, T. T., "Measurement of Air Flow Characteristics Using Seven-Hole Cone Probes," NASA TM-112194, May 1997.

[19]Shepherd, I. C., "A Four Hole Pressure Probe for Fluid Flow Measurements in Three Dimensions," *Journal of Fluids Engineering*, Vol. 103, Dec. 1981, pp. 590–594.

[20]Ramakrishnan, V., "Calibration and Data Reduction Algorithms for Nonconventional Multi-Hole Pressure Probes," M.S. Thesis, Dept. of Aerospace Engineering, Texas A&M Univ., College Station, TX, May 2004, pp. 41–49.

[21]White, F. M., "Laminar Boundary Layers," *Viscous Fluid Flow*, 2nd ed., McGraw–Hill, New York, 1991, p. 298.

W. Ng
Associate Editor